Oriented Growth of Al_2O_3:ZnO Nanolaminates for Use as Electron-Selective Electrodes in Inverted Polymer Solar Cells

*Hyeunseok Cheun, Canek Fuentes-Hernandez, Jaewon Shim, Yunnan Fang, Ye Cai, Hong Li, Ajaya K. Sigdel, Jens Meyer, Julia Maibach, Amir Dindar, Yinhua Zhou, Joseph J. Berry, Jean-Luc Bredas, Antoine Kahn, Kenneth H. Sandhage, and Bernard Kippelen**

Atomic layer deposition is used to synthesize Al_2O_3:ZnO(1:*x*) nanolaminates with the number of deposition cycles, *x*, ranging from 5 to 30 for evaluation as optically transparent, electron-selective electrodes in polymer-based inverted solar cells. Al_2O_3:ZnO(1:20) nanolaminates are found to exhibit the highest values of electrical conductivity (1.2×10^3 S cm^{-1}; more than six times higher than for neat ZnO films), while retaining a high optical transmittance (≥80% in the visible region) and a low work function (4.0 eV). Such attractive performance is attributed to the structure (ZnO crystal size and crystal alignment) and doping level of this intermediate Al_2O_3:ZnO film composition. Polymer-based inverted solar cells using poly(3-hexylthiophene) (P3HT):phenyl-C_{61}-butyric acid methyl ester (PCBM) mixtures in the active layer and Al_2O_3:ZnO(1:20) nanolaminates as transparent electron-selective electrodes exhibit a power conversion efficiency of 3% under simulated AM 1.5 G, 100 mW cm^{-2} illumination.

1. Introduction

By eliminating the need for low work function metals, such as Ca or LiF/Al, polymer solar cells with transparent, oxide-based, electron-selective electrodes can exhibit significantly improved stability.[1–5] Indium tin oxide (ITO) processed in air has a work function between 4.6 and 4.7 eV and generally acts as a hole-collecting electrode in solar cells. However, ITO may be utilized as an electron-selective electrode if its work function is sufficiently reduced through appropriate surface modification (e.g., by coating ITO with a thin layer of a lower work function metal oxide, such as TiO_x, ZnO, or Al_2O_3[1,2,5–7]) Unfortunately, inverted solar cells using modified ITO electrodes have shown severely reduced fill factors, with corresponding reductions in power conversion efficiency, owing to the appearance of an s-shaped kink in the current–voltage characteristics, which is commonly associated with surface recombination.[8] Although such an s-shape kink may be removed by exposure to ultraviolet radiation or continuous electrical bias,[5,6,9] the need for post-fabrication treatments is not desirable.

We previously demonstrated that the work function of the transparent conducting oxide (TCO) amorphous-InZnO could be controlled by adjusting the oxygen level during processing, which then enabled the fabrication of inverted polymer solar cells without the need for an interlayer or post-fabrication treatments.[6] However, the high demand for indium in flat panel displays and other applications, and the associated high and rising price of indium, provide strong incentives to identify indium-free TCOs for polymer solar cells. While other impurity-doped ZnO TCOs,[10] such as Al-doped ZnO[11,12] and Ga-doped ZnO,[13] have been proposed in the literature as alternative TCOs, these materials have mostly been used in the context of organic light-emitting diodes. New indium-free TCOs that can serve as electron-selective electrodes with work functions lower than ITO, without the need for additional interlayers or undesired post-fabrication treatments, and with surface properties that result in kink-free current–voltage behavior (for large

Dr. H. Cheun, Dr. C. Fuentes-Hernandez, J. Shim, A. Dindar, Dr. Y. H. Zhou, Prof. B. Kippelen
Center for Organic Photonics and Electronics (COPE)
School of Electrical and Computer Engineering
Georgia Institute of Technology
Atlanta, GA 30332, USA
E-mail: kippelen@ece.gatech.edu

Dr. Y. Fang, Dr. Y. Cai, Prof. K. H. Sandhage
Center for Organic Photonics and Electronics (COPE)
School of Materials Science and Engineering
Georgia Institute of Technology
Atlanta, GA 30332, USA

Dr. H. Li, Prof. J. L. Bredas
Center for Organic Photonics and Electronics (COPE)
School of Chemistry and Biochemistry
Georgia Institute of Technology
Atlanta, GA 30332, USA

A. K. Sigdel, Dr. J. J. Berry
National Center for Photovoltaics,
National Renewable Energy Laboratory
Golden, CO 80401, USA

Dr. J. Meyer, J. Maibach, Prof. A. Kahn
Department of Electrical Engineering
Princeton University Princeton, NJ 08544, USA

DOI: 10.1002/adfm.201102968

fill-factors and high power conversion efficiencies) need to be developed.

A less explored class of TCOs consists of nanolaminates of different metal oxide layers synthesized by atomic layer deposition (ALD). The ALD method involves the use of self-limiting surface reactions that, in turn, allow for the well-controlled, layer-by-layer growth of uniform and highly conformal films.[14] Indeed, dielectric films processed by ALD have been shown to act as effective encapsulation layers (i.e., as excellent barriers to oxygen and water) for organic solar cells.[15] Furthermore, the recent demonstration of a high-speed ALD process that yields deposition rates of up to 1.2 nm s^{-1},[16] around two orders of magnitude improvement over typical deposition rates, highlights the potential of ALD to become a widespread industrial technique. While ALD-derived Al_2O_3:ZnO nanolaminates[17] have been used as transparent electrodes in organic light-emitting diodes[18] and thin-film transistors,[19] their use as electron-selective electrodes in organic solar cells remains to be explored.

The ALD process is well-suited for adjusting the relative thicknesses of alternating Al_2O_3 and ZnO layers, as well as the overall thickness of a conformal Al_2O_3:ZnO nanolaminate film. In the past, the interplay between the relative thickness of the Al_2O_3 and ZnO layers and the resulting electrical properties of Al_2O_3:ZnO nanolaminates have been primarily explained in terms of Al doping.[17,20–22] Interestingly, reports on the structural characteristics of these nanolaminate layers are somewhat contradictory; that is, some authors have found that changes in the relative thicknesses of the Al_2O_3 and ZnO layers resulted in changes in the X-ray diffraction (XRD) patterns, consistent with changes in the preferred ZnO growth orientation,[20] while others have not observed such a trend.[22] ZnO within polycrystalline films often forms with a hexagonal wurtzite structure and can exhibit a preferred orientation (i.e., with an *a* or *c* crystallographic axis preferentially aligned perpendicular to the substrate surface).[23] For instance, ZnO films have been deposited on single-crystal Al_2O_3[23] or SiO_2/Si[24] substrates with the ZnO basal plane preferentially oriented parallel to the substrate surface. However, the role of ultrathin Al_2O_3 layers (under 1 nm) within the Al_2O_3:ZnO nanolaminates on the crystallographic orientation of ZnO is unclear, with conflicting reports found in the literature.[22]

This work provides an evaluation of the structural, electrical, and optical properties of ALD-derived Al_2O_3:ZnO(1:*x*) nanolaminates, where *x* is the number of deposition cycles, and of the performance of inverted organic polymer solar cells utilizing such nanolaminates as transparent electron-selective electrodes. We show that the appropriate introduction of Al_2O_3 layers within Al_2O_3:ZnO(1:*x*) nanolaminates can result in the oriented growth of ZnO that, along with doping, results in a significant improvement in the electrical conductivity of the nanolaminates. We also demonstrate that the combined electrical, optical, and structural properties of these nanolaminates make them efficient electron-selective electrodes in poly(3-hexylthiophene) (P3HT):phenyl-C_{61}-butyric acid methyl ester (PCBM) polymer-based inverted solar cells; without further modification of their work function or post-fabrication treatments, these cells exhibit power conversion efficiency values of 3% under simulated AM 1.5G, 100 mW cm^{-2} illumination.

2. Results and Discussion

2.1. Oriented Growth

Before describing the syntheses and characterization of nanolaminate Al_2O_3:ZnO(1:*x*) films, the structure and properties of ZnO films (100 nm thick) prepared by ALD on glass and on Al_2O_3-coated glass substrates is discussed. In our notation, *x* refers to the number of deposition cycles of ZnO following a single deposition cycle of Al_2O_3. Unless specified, the first deposition cycle on a given substrate was a single cycle of Al_2O_3. Multiple cycles of Al_2O_3:ZnO(1:*x*) depositions were repeated until films with a total thickness of 100-200 nm were obtained. The Al_2O_3-coated glass substrates were prepared by using a single ALD cycle to deposit a thin (≈0.1 nm) Al_2O_3 coating onto the glass substrate. The XRD patterns obtained from ZnO films deposited on plain glass and on Al_2O_3-coated glass substrates are shown in **Figure 1**a. Comparison of the relative intensities of the (002) and (100) ZnO diffraction peaks indicates that the ZnO film deposited on Al_2O_3-coated glass has a greater degree of ZnO basal plane alignment parallel to the substrate surface than the ZnO film deposited directly on glass. Consistent with previous reports in the literature,[24] a relatively intense (002) diffraction peak is also detected for ZnO films grown on a SiO_2/Si(001) wafer substrate. The increased basal plane alignment of the ZnO crystallites is accompanied by changes in the conductivity of these films, as measured using the transfer length method (TLM).[25] The ZnO film deposited on the Al_2O_3-coated

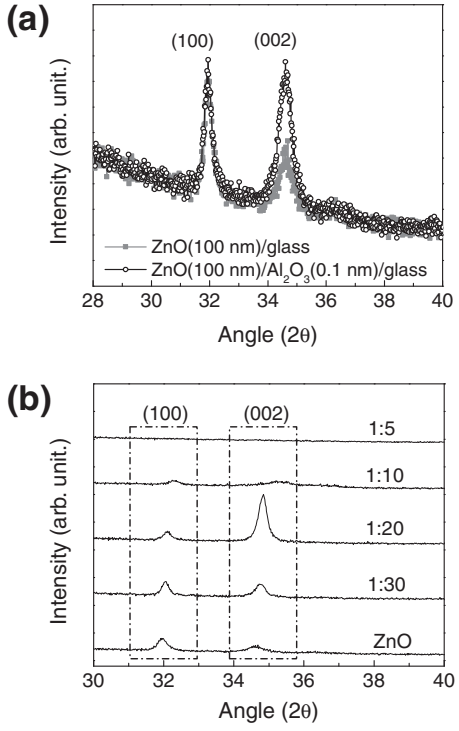

Figure 1. a) XRD analyses of 100 nm-thick ZnO films grown on a bare glass substrate and a Al_2O_3(0.1 nm)/glass substrate. b) XRD analyses of a 100-nm-thick ZnO film and 100-nm-thick Al_2O_3:ZnO(1:30), (1:20), (1:10), and (1:5) nanolaminate films on a glass substrate.

glass, exhibits a conductivity value of 240 ± 13 S cm^{-1}, which corresponded to a 30% improvement over the value exhibited by the ZnO film deposited directly on glass (181 ± 6 S cm^{-1}). This improvement of conductivity could be attributed to doping by the Al_2O_3 layer, or to the change in alignment of ZnO crystals in the film, or a combination of both effects. It is interesting to note that the ZnO film deposited on the SiO_2/Si(001) wafer substrate exhibits a conductivity of 241 ± 2 S cm^{-1}. For this film, doping of the ZnO by the substrate is very unlikely to have occurred. These very similar conductivity values suggest that the enhanced basal plane alignment observed for both films play an important role in the improved conductivity.

To further evaluate the relative roles of crystal orientation and doping, a third set of samples was fabricated. After depositing a 100-nm-thick ZnO film directly on the glass substrate, a single ALD cycle was used to deposit a coating of Al_2O_3 on top of the ZnO film. The conductivity of this Al_2O_3-coated ZnO film was found to be 180 ± 13 S cm^{-1}, which is indistinguishable from the conductivity of the pure ZnO film directly deposited on glass. Since the deposition of an Al_2O_3 coating on top of the ZnO film is unlikely to have affected the morphology of the underlying (previously deposited) ZnO, but could have resulted in doping of the ZnO layer, this result suggests that the role of Al_2O_3 doping on the conductivity of films with this geometry might be less important than the role of the Al_2O_3 on the orientation of crystals within the ZnO film.

The structure and properties of Al_2O_3:ZnO(1:*x*) nanolaminate films, prepared by sequential deposition of Al_2O_3 and ZnO layers of differing thickness onto glass substrates, were then examined. In contrast to previous studies[22] and following the observations discussed above, nanolaminates were grown by starting with a single cycle of Al_2O_3, instead of ZnO, on the glass substrates. Figure 1b shows XRD patterns obtained from a 100-nm-thick ZnO film and 100-nm-thick Al_2O_3:ZnO(1:*x*) nanolaminate films with various ALD cycle ratios (*x* = 30, 20, 10, and 5) on glass substrates. The average thickness of ZnO per deposition cycle on top of Al_2O_3 was estimated to be around 0.152 nm and 0.13 nm on top of glass. The intensity of the (100) diffraction peak detected for the pure ZnO film is higher than for the (002) diffraction peak. However, an increase in the overall number of deposited Al_2O_3 layers in the total film thickness, corresponding to a decrease in the ZnO:Al_2O_3 ratio to a value of *x* = 20, results in an increase in the relative intensity of the (002) ZnO diffraction peak. Further increases in the overall number of deposited Al_2O_3 layers (corresponding to *x* values of 10 and 5) lead to a significant decrease in the intensities of the (002) and (100) diffraction peaks. The average ZnO crystal size is also influenced by the total number of alumina layers in the films. Scherrer analyses of the (002) ZnO diffraction peaks yield average ZnO crystal sizes (**Table 1**) of 30 and 35 nm for the Al_2O_3:ZnO(1:30) and Al_2O_3:ZnO(1:20) films, respectively, while values of 17 nm and 9 nm are obtained for the ZnO and Al_2O_3:ZnO(1:10) films, respectively. XRD analyses of Al_2O_3:ZnO(1:*x*) nanolaminates deposited on SiO_2/Si(001) wafer substrates reveal trends similar to those observed for films on bulk glass substrates (Figure S1, Supporting Information).

The increase in the relative intensity of the (002) ZnO diffraction peak and in the average ZnO crystal size, upon periodic insertion of a single Al_2O_3 cycle throughout the Al_2O_3:ZnO(1:30) and Al_2O_3:ZnO(1:20) nanolaminate films, indicates that such interspersed Al_2O_3 layers act to promote the nucleation/growth of ZnO crystals with basal planes oriented parallel to the substrate surface; that is, these interspersed Al_2O_3 layers act in a similar manner as discussed above for a single Al_2O_3 layer deposited on the glass substrate. The significant reduction in the intensities of the (100) and (002) diffraction peaks in the Al_2O_3:ZnO(1:10) and Al_2O_3:ZnO(1:5) nanolaminates points to the existence of a critical number of ZnO deposition cycles required for the extensive nucleation and growth of ZnO crystals between the deposited Al_2O_3 layers. This observation is qualitatively consistent with the reports of Elam et al.[17] and Lee et al.[22] who found that a critical ZnO thickness is needed to generate Al_2O_3:ZnO nanolaminates with a high conductivity, although the latter authors attributed this behavior to the existence of a critical ZnO thickness between the Al_2O_3 layers needed to fully activate the extrinsic doping mechanism.

Table 1. Average ZnO crystal size for ZnO films and Al_2O_3:ZnO (1:x) nanolaminate films with various x values (x = 30, 20, 10, and 5) on glass substrates.

	(002) peak position, 2θ [°]	Crystal size[a)] [nm]	Conductivity[b)] [S cm^{-1}]
ZnO only	34.5	17	181 ± 6
1:30	34.5	30	1081 ± 27
1:20	34.5	35	1226 ± 41
1:10	35.4	9.1	202 ± 1
1:5	-	–	–

a) Average ZnO crystal size as determined by Scherrer analysis; b) Averaged over three measurements with the indicated error range corresponding to the standard deviation.

Selected-area electron diffraction (SAED) and high-resolution transmission electron microscopy (HRTEM) were also used for structural evaluation of the films. **Figure 2**,b illustrates the SAED patterns of ZnO films and Al_2O_3:ZnO(1:20) nanolaminates deposited on the SiO_2/Si(001) wafer substrates. For the ZnO film, a high degree of ZnO basal plane alignment parallel to the (002) planes of the Si substrate is not found. In contrast, for the Al_2O_3:ZnO(1:20) nanolaminates, relatively bright streaks are detected at (002) Si diffraction spots, which is consistent with a strong degree of ZnO basal plane alignment parallel to the SiO_2/Si(001) wafer surface. Figure 2c,d presents the HRTEM images of cross-sections of the ZnO film and the Al_2O_3:ZnO(1:20) nanolaminate, respectively, near the film/substrate interfaces. Lattice fringes seen in these HRTEM images reveal ZnO crystals with (100) planes (Figure 2c) and (002) planes (Figure 2d) oriented parallel (or nearly parallel) to the film/substrate interfaces.

Another important morphological characteristic of a transparent electrode for solar cell applications is the surface roughness. Values of root-mean-squared (RMS) surface roughness were obtained, by averaging over three areas on a given sample, from atomic force microscopy (AFM) images of different ALD-derived films (Figure S2, Supporting Information). The surface of the neat ZnO film is noticeably rougher (RMS surface roughness values of 2.4 nm) and contains some apparent

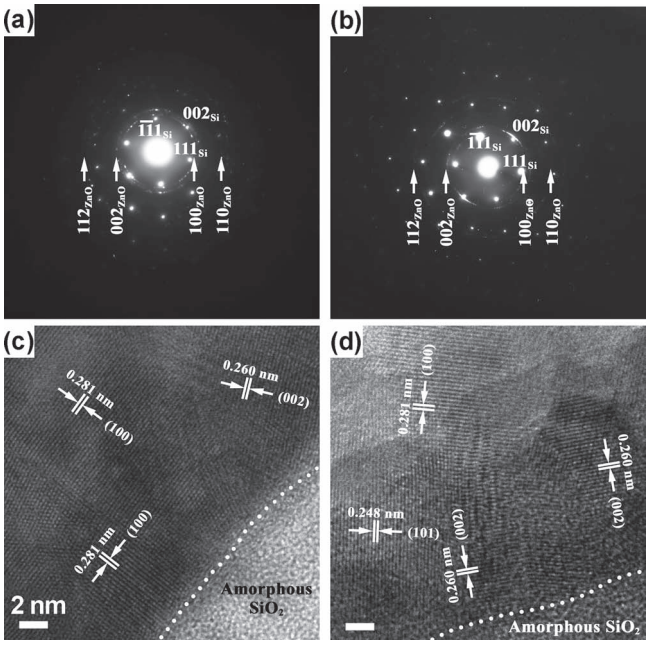

Figure 2. SAED patterns obtained from a) a 100-nm-thick ZnO film and b) a 100-nm-thick Al_2O_3:ZnO(1:20) nanolaminate film on a SiO_2/Si(001) wafer substrate. HRTEM images of cross-sections of c) a 100-nm-thick ZnO film and d) a 100-nm-thick Al_2O_3:ZnO(1:20) nanolaminate film on a SiO_2/Si(001) wafer substrate.

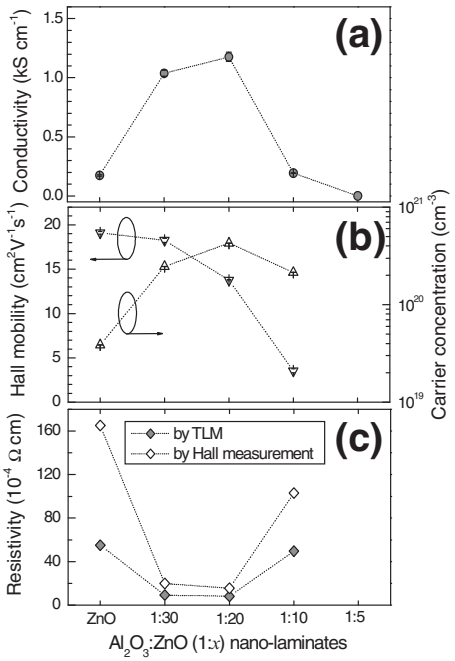

Figure 3. a) Conductivity values of a 100-nm-thick ZnO film and 100-nm-thick Al_2O_3:ZnO(1:30), (1:20), (1:10), and (1:5) nanolaminate films on a glass substrate measured by TLM. b) Hall mobility values and carrier concentrations of a 100-nm-thick ZnO film and 100-nm-thick Al_2O_3:ZnO(1:30), (1:20), and (1:10) nanolaminate films on a glass substrate. c) Resistivity values of nanolaminate films obtained by TLM and Hall mobility measurements.

particles that are larger than for the Al_2O_3:ZnO nanolaminate films. The average RMS surface roughness values of the Al_2O_3:ZnO nanolaminate films fall within the narrow range of 1.2 to 1.4 nm.

TLM measurements were conducted to correlate the structural analyses with the electrical properties of the ZnO and Al_2O_3:ZnO nanolaminate films. The values of conductivity obtained by TLM measurements are shown in **Figure 3**a and also summarized in Table 1. The initial rise in conductivity with an increase in the total relative number of Al_2O_3 layers (up to an x value of 20), followed by a sharp decrease in conductivity with additional Al_2O_3 layers (from x values of 20 down to 5), correlate well with the XRD analyses. Films with intense (002) ZnO diffraction peaks (relative to (100) diffraction peaks) exhibit relatively high values of conductivity. For instance, the highest conductivity of 1226 ± 41 S cm^{-1} (a value 6.8 times larger than the value of 181 ± 6 S cm^{-1} for neat ZnO films) is obtained in Al_2O_3:ZnO(1:20) nanolaminates with the most intense (002) diffraction peak.

To further investigate the origin of the enhanced conductivity in Al_2O_3:ZnO(1:20) nanolaminates and the significantly reduced values of conductivity for neat ZnO films and Al_2O_3:ZnO(1:10) and Al_2O_3:ZnO(1:5) nanolaminates, Van der Pauw method Hall measurements were conducted on these films. Figure 3b displays the carrier concentrations and mobility values of ZnO films and Al_2O_3:ZnO nanolaminates. Interestingly, while the mobility value measured in the ZnO film is 28% higher than for the Al_2O_3:ZnO(1:20) nanolaminate film, the carrier density of the latter film is an order of magnitude higher, which is likely to be attributed to a doping effect from the Al_2O_3 layers.

For the Al_2O_3:ZnO(1:20) nanolaminates that exhibit the highest electrical conductivity, a mobility value of 13.8 ± 0.1 cm^2 V^{-1} s^{-1} and a carrier concentration of 4.3×10^{20} cm^{-3} are measured. As shown in Figure 3c, the resistivity values extracted from Hall measurements experiments are slightly higher than the values obtained by TLM experiments. This discrepancy is attributed to differences in the lengths over which the conductivities of these samples were tested. In TLM measurements, the maximum separation distance between electrodes was 200 μm, while the typical electrode separation in the Hall mobility setup was ≈1.8 cm. Hence, carrier scattering at grain boundaries was expected to be more significant in Hall measurements than in TLM measurements, with a corresponding decrease in conductivity.

The measured values of the mobility and carrier concentration qualitatively follow the trend reported by Lee et al.[22] These authors assumed that a constant carrier concentration was introduced by each ZnO layer, regardless of the ZnO thickness, and that the carrier concentration introduced by Al_2O_3 could then be calculated as $\Delta c = c_{\text{nanolaminates}} - f_{\text{ZnO}} c_{\text{ZnO}}$, where c refers to the carrier concentration and f is the volume fraction. The carrier concentration per Al_2O_3 layer was then estimated as $N_l = d\Delta c/m$, where d is the film thickness and m the number of Al_2O_3 cycles. Following this analysis, it was estimated that for ZnO layers with a thickness above a critical value (2.5 nm) the average number of carriers introduced by each Al_2O_3 layer was constant (around 4.5×10^{13} carriers cm^{-2}). Below this critical thickness, the carrier concentration introduced by each Al_2O_3

layer dropped significantly (i.e., to a value of 2×10^{13} carriers cm^{-2} for ZnO layers with a thickness of ≈2 nm). Using the same analysis for the films investigated in the present work, the contribution of each Al_2O_3 layer added to the structure is estimated to be 1×10^{14} carriers cm^{-2} for the $x = 20$ and 30 nanolaminates (about a factor of two larger than reported by Lee et al.) and 3×10^{13} carriers cm^{-2} for the nanolaminates with $x = 10$. Although the precise doping mechanism is still under investigation, the higher doping efficiency by the Al_2O_3 layers observed in our nanolaminates could be related to the high degree of ZnO basal plane alignment oriented parallel to the substrate surface.

Another important aspect to consider for applications in solar cells is the optical transparency of the TCO. **Figure 4** illustrates the optical transmittance and optical band gap of a 300-nm-thick ZnO film and 300-nm-thick Al_2O_3:ZnO(1:30), (1:20), and (1:10) nanolaminates on a glass substrate. The optical bandgap values were estimated from the optical transmission spectra by extrapolating to zero the linear portion of the plot of the square of the absorption coefficient, α^2, versus photon energy, as shown in Figure 4b. In Figure 4a, all of the ZnO films and Al_2O_3:ZnO nanolaminates show a transmittance above 80% in the visible and near-infrared region, along with a sharp absorption band edge. The modulations observed in the transmittance are due to Fabry–Perot type interference fringes that arise within the nanolaminates. The optical bandgap of the neat ZnO film is found to be 3.28 eV, which is consistent with values found in the literature.[26,27] Interestingly, with a decrease of x (that is, with an increasing number of Al_2O_3 layers), the absorption band edge for all the nanolaminates undergoes a blue-shift. For instance, an optical bandgap value of 3.63 eV is obtained for the Al_2O_3:ZnO(1:10) nanolaminates, which represents a shift of 0.35 eV from the bulk ZnO optical bandgap.

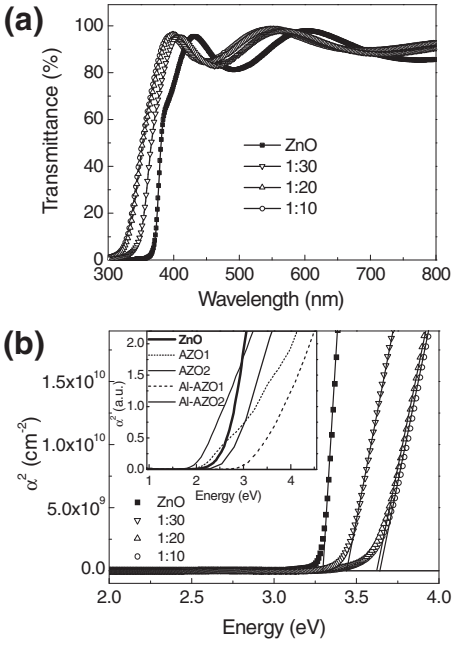

Figure 4. a) Optical transmission and b) square of the absorption coefficient of a 300-nm-thick ZnO film and 300-nm-thick Al_2O_3:ZnO(1:30), (1:20), and (1:10) nanolaminate films on a glass substrate. The inset shows the simulated square of the absorption coefficient of nanolaminate structures AZO1, AZO2, Al-AZO1, and Al-AZO2.

In order to gain a better understanding of the optical absorption data, we carried out density functional theory (DFT) calculations. To model the ALD-derived nanolaminates, we considered multilayer aluminum oxide/zinc oxide structures, corresponding to the Al_2O_3:ZnO(1:10) or Al_2O_3:ZnO(1:20) nanolaminates. We evaluated the electronic properties of: i) structures in which a fully coordinated Al_2O_3 layer is inserted between the ZnO layers (these structures are denoted AZO-1, with a composition corresponding to $Al_4Zn_{20}O_{26}$ per unit cell, and AZO-2, corresponding to $Al_4Zn_{40}O_{46}$) and ii) structures where an extra Al atom substitutes a Zn atom in the ZnO layer next to the Al_2O_3 layer (Al-AZO-1, corresponding to $Al_5Zn_{19}O_{26}$, and Al-AZO-2, corresponding to $Al_5Zn_{39}O_{46}$). The crystal structures and optical absorption spectra calculated for these four multi-layer films are then compared to those obtained for bulk ZnO.

The optical absorption spectra were evaluated in the framework of direct (vertical) single-particle transitions from the valence bands to the empty (parts of the) conduction bands for bulk ZnO and the multilayer Al_2O_3:ZnO structures (see the inset of Figure 4b). It must be borne in mind that since the DFT-calculated bandgaps of semiconductors are usually underestimated, it is more relevant to consider the trends in bandgap shifts rather than the absolute values. For the ZnO crystal, a direct bandgap of 1.77 eV is calculated and can be related to the optical absorption onset. In the case of the structures with a fully coordinated Al_2O_3 layer, AZO-1 and AZO-2, indirect bandgaps of 1.20 eV and 1.23 eV are obtained, respectively. The lowest direct energy gaps, which define the onsets of optical absorption in both structures, are calculated to be 1.50 eV and 1.53 eV, respectively. Clearly, when considering structures AZO-1 and AZO-2, we obtain a red-shift in optical gap, a result opposite to the trend observed experimentally (Figure 4b).

For structures Al-AZO-1 and Al-AZO-2, where an additional Al atom is present per unit cell and substitutes a Zn atom in the ZnO layer next to the Al_2O_3 layer, the Fermi levels are shifted above the bottom of the conduction band, which is consistent with metallic-type conductivity. In this case, the calculated optical absorptions (inset of Figure 4b) displays significant blue-shifts with respect to the pure ZnO crystal, on the order of 0.71 eV in Al-AZO-1 and 0.23 eV in Al-AZO-2. While these shifts are larger than the values observed experimentally, the increase in optical gap with Al doping is consistent with the experimental trend. Such changes can be attributed to shifts of the Fermi energy into the conduction band of the semiconductor as the level of carriers is increased through doping (an effect referred to as the Burstein–Moss effect).[28,29] However, Valle et al. also suggested that bandgap widening could arise from quantum confinement effects in samples containing relatively small crystallites (20 nm).[30] Because such crystallite sizes are on the same order of magnitude as our estimations of the ZnO grain size from Scherrer analyses of the XRD data (30–35 nm), contributions from such quantum confinement effects cannot be ruled out.

Finally, the electronic structure of 6 nm-thick Al_2O_3, ZnO, and Al_2O_3:ZnO films were measured via ultraviolet spectroscopy (UPS) and inverse photoemission spectroscopy (IPES). All

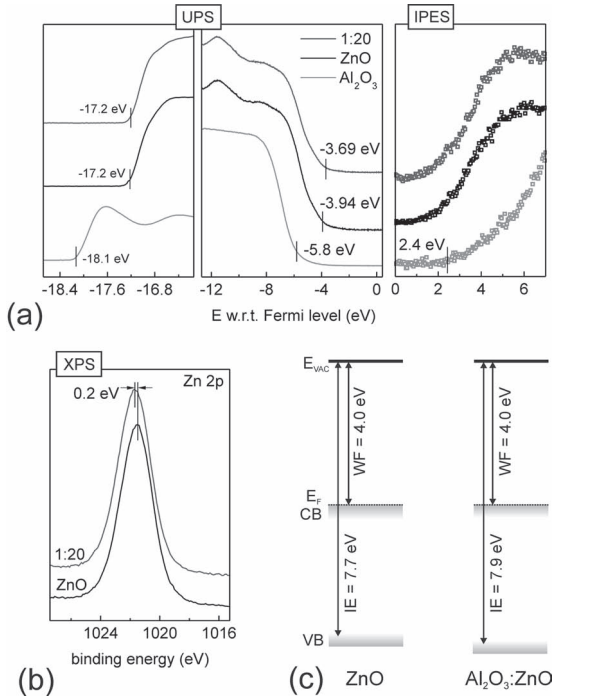

Figure 5. a) UPS and IPES data for ZnO, Al_2O_3 and Al_2O_3:ZnO(1:20) nanolaminate films on a glass substrate. b) Comparison of the Zn 2p in ZnO and Al_2O_3:ZnO(1:20) nanolaminate films measured by XPS. c) Energy band diagram of ZnO and Al_2O_3:ZnO(1:20) nanolaminate films derived from UPS and IPES spectra.

samples were deposited at 200 °C on Si substrates. **Figure 5**a exhibits the combined UPS and IPES data plotted with respect to the Fermi level. It can be seen that both ZnO and Al_2O_3:ZnO yield a photoemission onset at 17.2 eV, which corresponds to a work function (WF) of 4.0 ± 0.2 eV. Similar experiments on films deposited on glass substrates and with thicknesses in the range between 10 nm and 200 nm yielded the same values, with variations within the resolution of our setup. However, in thicker films and particularly in ZnO films, charging was observed during the UPS measurements. These effects were avoided with the use of the conductive Si substrates and thinner (6 nm) films. Similar WF values of 4.2 ± 0.1 eV were determined by Kelvin probe measurements in air for the 300 nm-thick Al_2O_3:ZnO(1:*x*) nanolaminates, with no appreciable variations found with increasing Al_2O_3 content (decreasing *x* value) of the films. These work function values are also in good agreement with previous reports on ALD-grown ZnO.[6]

A closer look at the density of states near the valence band (VB) top reveals that the addition of the Al_2O_3 layers in the ZnO film shifts the VB edge (0.25 eV) away from the Fermi level, while at the same time a higher density of unoccupied states can be observed close to the Fermi level. Note that Al_2O_3 is a wide bandgap material that shows no features near the Fermi level in the UPS/IPES spectra that could lead to the observed shift. In addition, the X-ray photoelectron spectra (XPS) spectra of the Zn 2p core level, as shown in Figure 5b, confirm the shift towards higher binding energy for the Al_2O_3:ZnO nanolaminate sample. As previously shown with DFT calculations, Al doping of ZnO raises the Fermi level above the conduction band minimum, leading to a strongly degenerated film. The observed shift of the UPS and XPS spectra and the higher density of unoccupied states near the Fermi level confirm that Al acts as an n-type dopant in the ZnO lattice and leads to a filling of the conduction band states. Interestingly, the UPS/IPES study suggest that our neat ZnO films are also strongly degenerate, most likely as a result of n-type doping via oxygen vacancies, which is supported by the high carrier concentration of around 3.9×10^{19} cm^{-3}. Figure 5c summarizes the energy levels of the ZnO and Al_2O_3:ZnO nanolaminate films. Since the exciton binding energy in ZnO is 60 meV[31] and the optical bandgap is 3.30 eV, we can estimate the conduction band (CB) edge to be around 0.4 eV below the Fermi level. We note that, within the experimental error (<0.05 eV), the optical bandgap of ZnO films does not show any thickness dependence. The 0.25 eV increase in ionization energy (IE) due to Al n-type doping suggest that also the bandgap increases as well, which is in excellent agreement with our optical and theoretical studies.

2.2. Inverted Solar Cells

The high optical transmittance in the visible and near infrared region, high conductivity, low surface roughness, and low work function make these Al_2O_3:ZnO(1:20) nanolaminates excellent candidates for electron-selective electrodes in inverted polymer solar cells. To demonstrate their potential, inverted polymer solar cells were fabricated with the structure: glass/Al_2O_3:ZnO(1:20) nanolaminates/P3HT:PCBM/poly(3,4-ethylenedioxythiophene):poly(styrenesulfonate) (PEDOT:PSS)/Ag. The photovoltaic

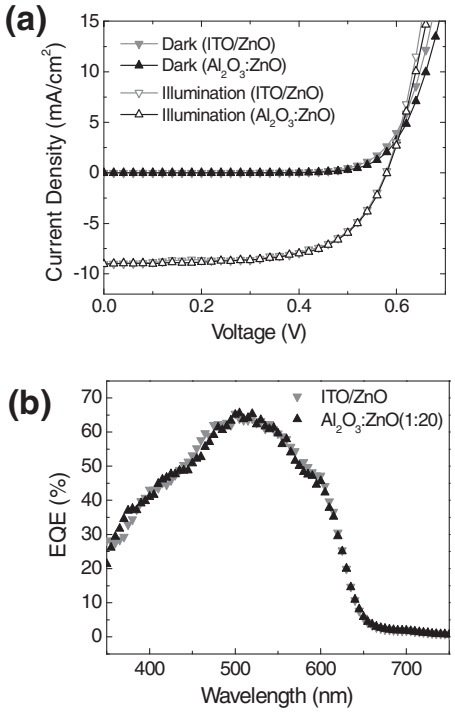

Figure 6. a) *J–V* characteristics and b) EQE for inverted devices, P3HT:PCBM/PEDOT:PSS/Ag, with Al_2O_3:ZnO(1:20) nanolaminate electrodes and ITO/ZnO electrodes.

Table 2. Average performance of inverted devices, P3HT:PCBM/PEDOT:PSS/Ag, with Al_2O_3:ZnO(1:20) nanolaminate electrodes or ITO/ZnO electrodes.

Transparent electrode	V_{OC}[a)] [mV]	J_{SC}[a)] [mA cm^{-2}]	FF[a)]	PCE[a,b)] [%]	Corrected PCE[c)] [%]
ITO/ZnO	590 ± 13	8.6 ± 0.3	0.63 ± 0.01	3.2 ± 0.1	3.0 ± 0.1
Al_2O_3:ZnO(1:20) nanolaminates	590 ± 5	8.7 ± 0.7	0.63 ± 0.01	3.2 ± 0.3	3.1 ± 0.3

[a)]Average obtained over four or five devices; [b)]PCE: power conversion efficiency; [c)]A 0.95 correction factor was applied to PCE on the basis of the spectral mismatch.

performance of these inverted devices was compared with those of reference devices using ITO/ZnO as a transparent electron-selective electrode. **Figure 6**a displays the current–voltage (J–V) characteristics in the dark and under illumination measured on both inverted solar cell devices. **Table 2** summarizes the photovoltaic performance averaged over four or five devices of each type. Devices with the Al_2O_3:ZnO(1:20) nanolaminates exhibit comparable values of fill-factor (FF = 0.63 ± 0.01), open-circuit voltage (V_{OC} = 590 ± 5 mV), and short-circuit current (J_{SC} = 8.7 ± 0.7 mA cm^{-2}), relative to the reference ITO/ZnO-based devices. These values yield an average power conversion efficiency of 3.2 ± 0.3%. Figure 6b shows that the EQE values for devices with the Al_2O_3:ZnO(1:20) nanolaminates and ITO/ZnO electrodes are similar. Based on the external quantum efficiency (EQE) spectra, a spectral mismatch factor of 0.95 was calculated for the Al_2O_3:ZnO(1:20) nanolaminates-based devices illuminated with our solar simulator.[5] Corrected power conversion efficiency values for AM1.5G illumination based on corresponding adjustments made to the photocurrent are summarized in Table 2. Importantly, such a performance level is obtained without the need for any post-fabrication treatment. Finally, it is also worth noting that, although the barrier properties of these nanolaminates were not investigated here, our previous results[15] suggest that ALD-grown films with thicknesses greater than 100 nm should exhibit excellent encapsulation properties. Hence, the nanolaminate films in the present work could serve a dual role in solar cells, organic light-emitting diodes, and other organic optoelectronic devices, as highly conductive transparent electrodes and as encapsulation layers.

3. Conclusion

The structural, electrical, and optical properties of Al_2O_3:ZnO(1:x) nanolaminates deposited by atomic layer deposition have been examined as a function of the relative number of ZnO deposition cycles. A seven-fold increase in electrical conductivity was achieved with Al_2O_3:ZnO(1:20) nanolaminates compared to neat ZnO films fabricated by ALD. This enhancement is attributed to a combination of structural changes (alignment and average size of the ZnO crystals) and doping effects. Al_2O_3:ZnO(1:20) nanolaminates on a glass substrate possess a high optical transmittance (≥80%) in the visible region and a blue-shifted optical bandgap, which increased the range of optical transparency by 0.35 eV with respect to ZnO, along with a high electrical conductivity (1226 ± 41 S cm^{-1}) and a low work function (4.0 ± 0.1 eV). P3HT:PCBM polymer-based inverted solar cells containing Al_2O_3:ZnO(1:20) nanolaminate electrodes exhibit power conversion efficiency values of 3% under simulated AM 1.5G, 100 mW cm^{-2} illumination.

4. Experimental Section

Film Preparation and Characterization: The deposition of Al_2O_3:ZnO nanolaminates was conducted in an ALD system (Savannah 100, Cambridge NanoTech, Cambridge, MA) on glass (Corning 1737, Corning Inc., Corning, NY) or on SiO_2(200 nm)/Si(001) wafer (F-755-007-A, Silicon Quest International, Inc., Santa Clara, CA) substrates. The glass and SiO_2/Si wafer substrates were cleaned sequentially in an ultrasonic bath of deionized water, acetone, and isopropyl alcohol and then loaded in the reactor in the ALD system. One ZnO ALD cycle consisted of sequential pulses of H_2O (15 ms pulse) and diethylzinc (15 ms pulse) precursors injected into the ALD reactor using nitrogen as a carrier gas at 200 °C. For a given Al_2O_3 cycle, trimethylaluminum (15 ms pulse) and H_2O (15 ms pulse) were used as precursors. Al_2O_3:ZnO nanolaminate films of 100 nm and 300 nm thickness were processed with a series of ZnO cycles with interspersed Al_2O_3 cycles incorporated at a given ratio (i.e., Al_2O_3:ZnO cycle ratios = 1:5, 1:10, 1:20, and 1:30). ZnO films of 100 and 300 nm thickness were also prepared for comparison with Al_2O_3:ZnO nanolaminate films.

The conductivity values of Al_2O_3:ZnO nanolaminates were obtained by transfer length method.[25] Measurements of Hall mobility and carrier concentration were conducted with a Hall measurement system (HL5500PC, Bio-Rad, Hercules, CA) with a buffer amplifier (HL5580, Bio-Rad, Hercules, CA). The structure of Al_2O_3:ZnO nanolaminates was characterized by X-ray diffraction, with Cu Kα radiation using an X-Pert Pro Alpha 1 diffractometer and an X'Celerator linear detector (PANalytical, Almelo, The Netherlands) and by high resolution transmission electron microscopy (TEM) (JEM 4000 EX, JEOL, Tokyo, Japan). The surfaces of Al_2O_3:ZnO nanolaminates were characterized by AFM (Dimension 3100 MultiMode AFM, NanoScope III controller, Veeco) under atmospheric conditions. Optical transmission spectra of Al_2O_3:ZnO nanolaminates on glass substrates were obtained using a UV–vis spectrometer (Cary 5E, Varian, Palo Alto, CA) and a reference glass substrate. The work function of Al_2O_3:ZnO nanolaminates on glass substrates was measured in air using a Kelvin probe (Kelvin probe S, Besocke Delta Phi, Germany). A highly oriented pyrolytic graphite (HOPG) sample with a work function of 4.5 eV was used as the reference. In UPS experiments, both He I (21.22 eV) and He II (40.8 eV) radiation lines from a discharge lamp were employed, with an experimental resolution of 0.15 eV. IPES was carried out in the isochromat mode, with a resolution of 0.45 eV.[32] The Fermi level reference was established by UPS and IPES measurements on a freshly evaporated Au surface. The core levels were studied by XPS using the Al $K\alpha$ (1486.6 eV) photon line with a spectral resolution of 0.8 eV.

Calculations of Electronic Structure: All calculations were carried out using the Vienna Ab Initio Simulation Package (VASP)[33,34] with the projector-augmented wave (PAW) method[35] and the generalized gradient approximation functional of Perdew, Burke, and Ernzerhof (PBE).[36] The LDA+U method[37] with U = 8.5 eV[38] was employed to describe the strong Coulomb repulsion on the highly localized Zn 3d electrons. A plane wave energy cut-off of 400 eV was applied for all elements and a total energy convergence of 10^{-6} eV was used for self-consistency of the iteration procedures. The geometry optimizations of the multilayer AZO and ZnO crystal structures involved full relaxation of the atomic coordinates with a residual-force minimization of 0.01 eV Å^{-1}, while the lattice parameters were fixed at the experimental values for the pure ZnO crystal.

Device Fabrication: Inverted polymer solar cells were fabricated on patterned Al_2O_3:ZnO(1:20) nanolaminates on glass substrates with active layers composed of polymeric blends of the donor polymer P3HT (4002E, Rieke Metals, Lincoln, NE) with the acceptor PCBM (Nano-C, Westwood, MA). ZnO-modified ITO films on glass substrates were used

in reference devices. These reference films consisted of a 20-nm-thick ZnO layer deposited on an ITO substrate (Colorado Concept Coatings LLC) by ALD at 200 °C. The nanolaminates were cleaned sequentially in an ultrasonic bath of deionized water, acetone, and isopropyl alcohol. P3HT:PCBM films were spin-coated on Al_2O_3:ZnO(1:20) nanolaminates and ITO/ZnO substrates for 1 min at 700 rpm from a solution comprised of a mixture of P3HT and PCBM in chlorobenzene (P3HT:PCBM weight ratio = 1:0.7; total P3HT + PCBM concentration = 34 mg mL^{-1}). These solutions were filtered through 0.2-µm-pore polytetrafluoroethylene (PTFE) filters prior to spin coating and the resulting samples were annealed at 160 °C for 10 min on a hot plate in a nitrogen-atmosphere glove box. PEDOT:PSS (CPP 105 DM, H.C. Starck, Newton, MA) was then spin-coated on top of the active layer at 5000 rpm for 1 min in air, followed by annealing at 120 °C for 10 min in the glove box. After loading the samples into a vacuum thermal evaporation system (SPECTROS, Kurt J. Lesker, Clairton, PA) connected to the glove box, a 150 nm-thick layer of Ag was deposited on the PEDOT:PSS layer through a shadow mask at a rate of 0.1–0.3 nm and a base pressure of 2×10^{-7} Torr. The completed devices were transferred in a sealed container to another nitrogen-filled glove box for electrical measurements. The active device area was 0.1 cm^2. Current–voltage characteristics were measured using a source meter (2400, Keithley Instruments, Cleveland, OH) controlled by a LabVIEW program. For illumination, an AM1.5G solar simulator (Oriel 91160, Oriel Instruments, Stratford, CT) with an irradiance of I_L = 100 mW cm^{-2} was used in the glove box. A monochromator coupled to a 175 W xenon lamp (ASB-XE-175EX, CVI Spectral Products, Putnam, CT) and a calibrated photodiode (S2386-44K, Hamamatsu, Japan) were used to measure the EQE.

Supporting Information

Supporting Information is available from the Wiley Online Library or from the author.

Acknowledgements

This work was funded in part through the Center for Interface Science: Solar Electric Materials, an Energy Frontier Research Center funded by the U.S. Department of Energy, Office of Science, Office of Basic Energy Sciences under Award Number DE-SC0001084 (H.C, Y.Z., B.K., J.Me., J.Ma., A.K.S., J.J.B, J.L.B, H.L.), by the STC Program of the National Science Foundation under Agreement No. DMR-0120967 (C.F.-H., A.D.), by AFOSR (BIONIC Center grant No. FA9550-09-1-0162) (Y.F., Y.C., K.H.S.), and by the Office of Naval Research (Grant No. N00014-04-1-0120) (J.S.), and by the National Science Foundation (DMR-1005892) (A.K.). This work was performed in part at the Microelectronics Research Center at Georgia Institute of Technology, a member of the National Nanotechnology Infrastructure Network, which is supported by NSF (Grant No. ECS- 03-35765). J.Me. acknowledges the Deutsche Forschungsgemeinschaft (DFG) for generous support within the postdoctoral fellowship program.
This article was amended on April 10, 2012 to correct an error in the version originally published online. Figure 5 was corrected to include all panels.

Received: December 7, 2011
Published online: February 1, 2012

[1] C. Waldauf, M. Morana, P. Denk, P. Schilinsky, K. Coakley, S. A. Choulis, C. J. Brabec, *Appl. Phys. Lett.* **2006**, *89*, 233517.
[2] M. S. White, D. C. Olson, S. E. Shaheen, N. Kopidakis, D. S. Ginley, *Appl. Phys. Lett.* **2006**, *89*, 143517.
[3] G. Li, C.-W. Chu, V. Shrotriya, J. Huang, Y. Yang, *Appl. Phys. Lett.* **2006**, *88*, 253503.
[4] S. K. Hau, H. L. Yip, N. S. Baek, J. Y. Zou, K. O'Malley, A. K. Y. Jen, *Appl. Phys. Lett.* **2008**, *92*, 253301.
[5] H. Cheun, J. B. Kim, Y. H. Zhou, Y. N. Fang, A. Dindar, J. Shim, C. Fuentes-Hernandez, K. H. Sandhage, B. Kippelen, *Opt. Express* **2010**, *18*, A506.
[6] H. Cheun, C. Fuentes-Hernandez, Y. H. Zhou, W. J. Potscavage, S. J. Kim, J. Shim, A. Dindar, B. Kippelen, *J. Phys. Chem. C* **2010**, *114*, 20713.
[7] R. Po, C. Carbonera, A. Bernardi, N. Camaioni, *Energy Environ. Sci.* **2010**, *4*, 285.
[8] A. Wagenpfahl, D. Rauh, M. Binder, C. Deibel, V. Dyakonov, *Phys. Rev. B* **2010**, *82*, 115306.
[9] T. Kuwabara, Y. Kawahara, T. Yamaguchi, K. Takahashi, *ACS Appl. Mater. Interfaces* **2009**, *1*, 2107.
[10] H. Kim, J. S. Horwitz, W. H. Kim, A. J. Mäkinen, Z. H. Kafafi, D. B. Chrisey, *Thin Solid Films* **2002**, *420-421*, 539.
[11] K. Schulze, B. Maennig, K. Leo, Y. Tomita, C. May, J. Hupkes, E. Brier, E. Reinold, P. Bauerle, *Appl. Phys. Lett.* **2007**, *91*, 073521.
[12] J. Meyer, P. Gorrn, S. Hamwi, H. H. Johannes, T. Riedl, W. Kowalsky, *Appl. Phys. Lett.* **2008**, *93*, 073308.
[13] J. Owen, M. S. Son, K. H. Yoo, B. D. Ahn, S. Y. Lee, *Appl. Phys. Lett.* **2007**, *90*, 033512.
[14] X. H. Zhang, B. Domercq, X. D. Wang, S. Yoo, T. Kondo, Z. L. Wang, B. Kippelen, *Org. Electron.* **2007**, *8*, 718.
[15] W. J. Potscavage, S. Yoo, B. Domercq, B. Kippelen, *Appl. Phys. Lett.* **2007**, *90*, 253511.
[16] P. Poodt, A. Lankhorst, F. Roozeboom, K. Spee, D. Maas, A. Vermeer, *Adv. Mater.* **2010**, *22*, 3564.
[17] J. W. Elam, S. M. George, *Chem. Mater.* **2003**, *15*, 1020.
[18] S. H. K. Park, J. I. Lee, C. S. Hwang, H. Y. Chu, *Jpn. J. Appl. Phys. Part 2* **2005**, *44*, L242.
[19] S. H. K. Park, C. S. Hwang, H. Y. Jeong, H. Y. Chu, K. I. Cho, *Electrochem. Solid State Lett.* **2008**, *11*, H10.
[20] J. W. Elam, D. Routkevitch, S. M. George, *J. Electrochem. Soc.* **2003**, *150*, G339.
[21] J. S. Na, G. Scarel, G. N. Parsons, *J. Phys. Chem. C* **2010**, *114*, 383.
[22] D. J. Lee, H. M. Kim, J. Y. Kwon, H. Choi, S. H. Kim, K. B. Kim, *Adv. Funct. Mater.* **2011**, *21*, 448.
[23] U. Ozgur, Y. I. Alivov, C. Liu, A. Teke, M. A. Reshchikov, S. Dogan, V. Avrutin, S. J. Cho, H. Morkoc, *J. Appl. Phys.* **2005**, *98*, 103.
[24] W. C. Shih, H. Y. Su, M. S. Wu, *Thin Solid Films* **2009**, *517*, 3378.
[25] R. Jackson, S. Graham, *Appl. Phys. Lett.* **2009**, *94*, 012109.
[26] S. J. Pearton, D. P. Norton, K. Ip, Y. W. Heo, T. Steiner, *J. Vac. Sci. Technol. B* **2004**, *22*, 932.
[27] V. Srikant, D. R. Clarke, *J. Appl. Phys.* **1998**, *83*, 5447.
[28] E. Burstein, *Phys. Rev.* **1954**, *93*, 632.
[29] T. S. Moss, *Proc. Phys. Soc. London Sect. B* **1954**, *67*, 775.
[30] G. G. Valle, P. Hammer, S. H. Pulcinelli, C. V. Santilli, *J. Eur. Ceram. Soc.* **2004**, *24*, 1009.
[31] E. O. Kane, *Phys. Rev. B* **1978**, *18*, 6849.
[32] J. Hwang, A. Wan, A. Kahn, *Mater. Sci. Eng. R* **2009**, *64*, 1.
[33] G. Kresse, J. Furthmüller, *Phys. Rev. B* **1996**, *54*, 11169.
[34] G. Kresse, J. Furthmüller, *Comput. Mater. Sci.* **1996**, *6*, 15.
[35] P. E. Blöchl, *Phys. Rev. B* **1994**, *50*, 17953.
[36] J. P. Perdew, K. Burke, M. Ernzerhof, *Phys. Rev. Lett.* **1996**, *77*, 3865.
[37] S. L. Dudarev, G. A. Botton, S. Y. Savrasov, C. J. Humphreys, A. P. Sutton, *Phys. Rev. B* **1998**, *57*, 1505.
[38] P. Palacios, K. Sánchez, P. Wahnón, *Thin Solid Films* **2009**, *517*, 2448.